Chemical Science

ROYAL SOCIETY OF CHEMISTRY

EDGE ARTICLE

Cite this: *Chem. Sci.*, 2023, **14**, 2009

All publication charges for this article have been paid for by the Royal Society of Chemistry

Microstructure-driven annihilation effects and dispersive excited state dynamics in solid-state films of a model sensitizer for photon energy up-conversion applications†

Hossein Goudarzi,[a] Loukas Koutsokeras,[b] Ahmed H. Balawi,[c] Chen Sun,[d] Giorgos K. Manolis,‡[e] Nicola Gasparini,[cf] Yuan Peisen,[b] Giannis Antoniou,[b] Stavros Athanasopoulos,[g] Charalampos C. Tselios,[h] Polycarpos Falaras,[e] Constantinos Varotsis,[h] Frédéric Laquai,[c] Juan Cabanillas-González[d] and Panagiotis E. Keivanidis*[b]

Bimolecular processes involving exciton spin-state interactions gain attention for their deployment as wavelength-shifting tools. Particularly triplet–triplet annihilation induced photon energy up-conversion (TTA-UC) holds promise to enhance the performance of solar cell and photodetection technologies. Despite the progress noted, a correlation between the solid-state microstructure of photoactuating TTA-UC organic composites and their photophysical properties is missing. This lack of knowledge impedes the effective integration of functional TTA-UC interlayers as ancillary components in operating devices. We here investigate a solution-processed model green-to-blue TTA-UC binary composite. Solid-state films of a 9,10 diphenyl anthracene (DPA) blue-emitting activator blended with a (2,3,7,8,12,13,17,18-octaethyl-porphyrinato) Pt^{II} (PtOEP) green-absorbing sensitizer are prepared with a range of compositions and examined by a set of complementary characterization techniques. Grazing incidence X-ray diffractometry (GIXRD) measurements identify three PtOEP composition regions wherein the DPA:PtOEP composite microstructure varies due to changes in the packing motifs of the DPA and PtOEP phases. In Region 1 (≤2 wt%) DPA is semicrystalline and PtOEP is amorphous, in Region 2 (between 2 and 10 wt%) both DPA and PtOEP phases are amorphous, and in Region 3 (≥10 wt%) DPA remains amorphous and PtOEP is semicrystalline. GIXRD further reveals the metastable DPA-β polymorph species as the dominant DPA phase in Region 1. Composition dependent UV-vis and FT-IR measurements identify physical PtOEP dimers, irrespective of the structural order in the PtOEP phase. Time-gated photoluminescence (PL) spectroscopy and scanning electron microscopy imaging confirm the presence of PtOEP aggregates, even after dispersing DPA:PtOEP in amorphous poly(styrene). When arrested in Regions 1 and 2, DPA:PtOEP exhibits delayed PtOEP fluorescence at 580 nm that follows a power-law decay on the ns time scale. The origin of PtOEP delayed fluorescence is unraveled by temperature- and fluence-dependent PL experiments. Triplet PtOEP excitations undergo dispersive diffusion and enable TTA reactions that activate the first singlet-excited (S_1) PtOEP state. The effect is reproduced when PtOEP is mixed with a poly(fluorene-2-octyl) (PFO) derivative. Transient absorption measurements on PFO:PtOEP films find that selective PtOEP photoexcitation activates the S_1 of PFO within ~100 fs through an up-converted ^{3}(d, d*) Pt^{II}-centered state.

Received 22nd November 2022
Accepted 25th January 2023

DOI: 10.1039/d2sc06426j

rsc.li/chemical-science

[a]*Centre for Nano Science and Technology @PoliMi, Fondazione Istituto Italiano di Tecnologia, 20133 Milano, Italy*

[b]*Device Technology and Chemical Physics Laboratory, Department of Mechanical Engineering and Materials Science and Engineering, Cyprus University of Technology, 3041 Limassol, Cyprus*

[c]*King Abdullah University of Science and Technology (KAUST), KAUST Solar Center (KSC), Physical Sciences and Engineering Division (PSE), 23955-6900 Thuwal, Kingdom of Saudi Arabia*

[d]*IMDEA Nanoscience, Ciudad Universitaria de Cantoblanco, Calle Faraday 9, ES 28049 Madrid, Spain*

[e]*Institute of Nanoscience and Nanotechnology, NCSR "Demokritos", 15341 Agia Paraskevi, Athens, Greece*

[f]*Department of Chemistry, Centre for Processable Electronics, Imperial College London, W120BZ, UK*

[g]*Departamento de Física, Universidad Carlos III de Madrid, 28911 Leganés, Madrid, Spain*

[h]*Environmental Biocatalysis and Biotechnology Laboratory, Department of Chemical Engineering, Cyprus University of Technology, 3603 Limassol, Cyprus*

† Electronic supplementary information (ESI) available: Materials and Methods, SEM, GIXRD, Raman, FT-IR, PL, time-gated PL and TA data. See DOI: https://doi.org/10.1039/d2sc06426j

‡ Deceased.

Introduction

Next generation photon management strategies that can boost the performance of optoelectronic and photonic devices continue to surge in tandem with recent progress in the understanding of organic semiconductor spin-physics.[1–4] Smart wavelength-shifting techniques could be potentially applied through triplet–triplet annihilation induced photon energy up conversion (TTA-UC), a photophysical process that facilitates a low-to-high photon energy conversion under low photoexcitation intensities. From early on (ref. [5]) it became evident that TTA-UC shows potential to support the development of artificial photosynthetic platforms.[6–13] Owing to their easily executable and inexpensive processing protocols, solution processable TTA-UC solid-state mixtures prepared by using small molecular and macromolecular π-conjugated systems are ideal candidate systems to be used as TTA-UC interlayers for device applications.[14–16] The solution processable character of TTA-UC organic materials offers an attractive opportunity to complement the portfolio of other existing photon energy up-converting systems[17–21] and to avoid disruptions in the design of currently employed device architectures. Although the realization of TTA-UC layers as functional device components is lagging, encouraging results were recently presented on a green-to-blue model TTA-UC composite prepared by blending the green-absorbing (2,3,7,8,12,13,17,18-octaethyl-porphyrinato) Pt^{II} (PtOEP) square-planar sensitizer with the blue-light emitting 9,10 diphenyl anthracene (DPA) emitter, a polycyclic aromatic hydrocarbon derivative. In particular, a striking TTA-UC PL quantum yield ($PLQY_{UC}$) of 8% (out of maximum 50%) was reported for optimized large-area DPA:PtOEP films[22] that can be further improved with the aid of ceramic-based nanocomposite frameworks.[23]

Following the demonstration of TTA-UC in the solid state,[24–26] it was realized that several key challenges first needed to be overcome before employing TTA-UC in technologically important bio-inspired light-harvesting devices. The immobilization of sensitizer and emitter species in the spatially confined environment of a solid composite system enhances the occurrence of parasitic re-absorption of the emitter TTA-UC luminescence by the sensitizer component.[27–30] In addition, the physical blending of sensitizer and emitter species *via* solution processing exhibits solid films[27,31–34] with a microstructure that is drastically different to that found in the pigment–protein complexes of naturally occurring photosynthetic organisms. In cyanobacteria, algae and plants, exciton migration takes place uninterruptedly within multi-chromophoric aggregate ensembles embedded in the complex thylakoid membrane environment.[35–37] In contrast, several detrimental exciton dissipative processes are operative in TTA-UC solids that may funnel photoexcitations towards undesired excited state pathways. The structurally disordered microstructure of TTA-UC composites results in the diffusive trapping of the absorbed photon energy in aggregate[33,38] and excimer-like sites,[39] thereby impacting negatively on the TTA-UC process. Disorder[40] further affects the excited state manifolds of the emitter and sensitizer components[41] and increases the overall complexity in the accurate description of their excited state dynamics.[42]

Owing to their disordered configurational and packing motifs, synthetic organic semiconductors exhibit a broad density of states (DOS) distribution wherein the optically induced excitations migrate through a hopping process towards progressively lower energy sites.[43–45] According to the Gaussian disorder model,[46] when energetic disorder is comparable to thermal energy, photoexcitations in the DOS relax towards quasi-equilibrium in a dispersive manner. For emissive excitations this relaxation manifests in a power-law function that describes the photoluminescence (PL) kinetics of the photoexcited system.[38,47,48] Energetic disorder leads to the complex temperature dependent PL properties of the emissive species. The balance between thermally activated exciton diffusion in the DOS and radiative or non-radiative exciton deactivation[49–51] results in a deviation from the conventional Arrhenius-like trend. Abnormal temperature dependent TTA-UC PL intensity patterns have been observed both for the benchmark TTA-UC DPA:PtOEP system[39,52,53] and the class of unconventional TTA-UC composites where PtOEP is mixed with blue-light emitting poly(*para*-phenylene) polymers, *e.g.* poly(fluorene) (PF) derivatives.[54] Unlike DPA:PtOEP, TTA-UC in PF:PtOEP blends originates from TTA reactions in the PtOEP phase followed by energy transfer to the PF matrix.[55] Despite the different operational TTA-UC mechanisms in the two solid-state systems, their common temperature-dependent PL properties pinpoint that energetic disorder in the PtOEP phase influences similarly their TTA-UC PL response.

TTA-UC composites promise a simple and low-cost solution casting protocol that enables direct deposition of interlayers on device electrodes. In this aspect, progress is noted with the development of smart material processing strategies that allow for the successful translation of the TTA-UC process in rubbery materials[56,57] and alike soft matter environments[58–70] as well as in the crystalline state.[71,72] Meaningful guidelines are available for achieving orientational order,[73] suppressing the parasitic re-absorption losses,[28–30] and eliminating the TTA-UC energy quenching sites.[74] However, several issues remain elusive and require elaboration.

Firstly, not all proposed material design strategies are compatible with the fabrication protocols of devices able to generate photocurrent.[75] Power generating and light detecting organic optoelectronic circuits are mainly developed by sandwiching an organic semiconductor photoactive layer within a vertically stacked electrode configuration.[12,76] To engineer such a device geometry *via* TTA-UC, the integration of electrically conductive TTA-UC interlayers within the electronic device structure is required. Another challenge to be addressed relates to the different packing motifs that material components can adopt,[77,99] *i.e.* three different polymorphs exist for the DPA emitter.[78] Since high DPA contents are recommended for elevating the $PLQY_{UC}$ of DPA-based TTA-UC solid-state platforms,[42,79] deciphering the nature of the emitter polymorph species in the microstructure of the TTA-UC films is of high priority. Finally, a puzzling issue is the actual role of sensitizer aggregates in the optimum composition that allows for maximum TTA-UC efficiency. Early studies focusing on pristine DPA:PtOEP composites have identified a 2 wt% PtOEP content as most appropriate for optimum TTA-UC performance.[31]

Yet, recent reports on the same system propose the use of a much lower PtOEP content.[22] It remains unclear whether the use of a nominal wt% content alone can exclude the possibility of sensitizer aggregate formation, especially when the TTA-UC films are thermally processed.[53] The detection of PtOEP delayed fluorescence in as-spun films of the DPA:PtOEP composite system shows that TTA bimolecular reactions are operative in the PtOEP phase of the blend.[52] More recently, bimolecular annihilation reactions within triplet PtOEP physical dimers were shown to drive photocurrent generation in high open-circuit organic photodetector devices with PtOEP-only photoactive layers.[76] The correlation of TTA reactivity in triplet-excited sensitizers with the microstructure of TTA-UC composite systems warrants further exploration. Moreover, the role of the sensitizer aggregates requires special attention and a reliable metric to probe PtOEP aggregate formation in the solid state is sought.

In this work we focus on the as-spun state of composite DPA:PtOEP films. By combining spectroscopic and structural characterization in a systematic study, we set out to identify how the film microstructure of the composite influences the occurrence of TTA reactions in the PtOEP phase. This is a timely contribution given the strong interest on the use of metallorganic complexes in TTA-UC composites and organic light emitting diode devices.[80–84,100]

A set of material characterization experiments is applied on a range of composition dependent DPA:PtOEP composite films developed by solution processing. Grazing incidence X-ray diffractometry (GIXRD) measurements identify the dominant DPA polymorph in the DPA:PtOEP films. Scanning electron microscopy (SEM) imaging and UV-vis absorption spectroscopy reveal that the use of a nominal PtOEP wt% content is not a reliable metric to exclude PtOEP aggregate formation in the blends. Instead, FT-IR spectroscopy is proposed as a suitable probing technique to monitor the evolution of PtOEP aggregation in these systems. Time-gated PL spectroscopy is employed to monitor the PtOEP delayed fluorescence of the DPA:PtOEP system on the ns time scale. PtOEP delayed fluorescence is studied at temperatures between 100 and 290 K and it is found to be the product of bimolecular annihilation reactions between triplet PtOEP excitations in the aggregated PtOEP phase of the blend. The occurrence of annihilation-induced PtOEP delayed fluorescence is further verified in films where DPA is replaced by a poly(fluorene-2-octyl) (PFO) derivative.[54] The common power-law decay patterns observed in the PtOEP delayed fluorescence kinetics of the DPA:PtOEP and PFO:PtOEP films confirm the key role of the dispersive triplet PtOEP exciton relaxation within an energetically disordered triplet PtOEP manifold. Based on the transient absorption (TA) spectroscopic characterization of a doctor-bladed PFO:PtOEP film, the annihilation of triplet-excited PtOEP states is found to generate TTA-UC luminescence *via* an ultrafast PFO activation channel involving a Pt^{II}-centered $^3(d, d^*)$ state of the square-planar metallorganic PtOEP complex.

Results

The chemical structures of the materials used in this study are presented in Scheme 1.

UV-vis absorption spectroscopy

The tendency of PtOEP to form aggregates in solution-processed blend films was addressed by recording composition dependent UV-vis spectra of three different types of PtOEP-based systems. The local environment of PtOEP in these composites was varied by mixing PtOEP with (i) the photophysically inert matrix of atactic poly(styrene) (PS) and (ii) the DPA emitter. The PtOEP content in both PS:PtOEP and DPA:PtOEP films was increased progressively between 0.3 and 30 wt%. Ternary PS:DPA:PtOEP films were also produced by dispersing the binary DPA:PtOEP compositions in PS. For preparing all PS:DPA:PtOEP systems, the PS content was kept three times higher than the content of DPA and the wt% content of PtOEP was calculated with respect to DPA. All PS:PtOEP, DPA:PtOEP, and PS:DPA:PtOEP composite films were studied in their as-spun state. For reference purposes the UV-vis absorption spectrum of a dilute (1 μM) PtOEP solution in toluene was also recorded. Fig. 1 presents the overview of the acquired UV-vis spectra by focusing on the spectral range of 490–570 nm where the Q-band of PtOEP is located.[85]

Fig. 1 finds no significant differences in the absorption spectra of the PS:PtOEP (black lines) and PS:DPA:PtOEP (green lines) films as the PtOEP content increases. In stark contrast, gradual changes are observed in the spectra of the DPA:PtOEP films (red lines) at higher PtOEP loadings. The PtOEP Q-band at 536 nm red-shifts while a low energy absorption feature appears at 550 nm. Both observations are in good agreement with time-dependent density functional theory (TD-DFT) calculations on the formation of physical PtOEP dimer species by monomers positioned at close proximity in a slip-stacked arrangement.[76] The electronic interaction of adjacent PtOEP monomers results in the splitting of the excited state PtOEP levels together with a red-shift in the energy of the low energy electronic transitions.[73,86]

Solely based on the acquired UV-vis absorption spectra, one would suggest that in the DPA:PtOEP composite, aggregate species form only when the PtOEP content exceeds 0.3 wt% whereas both PS:PtOEP and PS:DPA:PtOEP systems are aggregate-free, owing to the beneficial effect of the PS binder. Aggregates however are clearly resolved in the SEM images (ESI Fig. S.1†) of all three types of systems. In the PS:PtOEP films, SEM imaging resolves aggregates when the PtOEP content surpasses 6 wt%. For the DPA:PtOEP films, aggregated features are observable already for PtOEP contents as low as 0.3 wt%. Regarding PS:DPA:PtOEP, the formation of aggregated features evolves progressively as the content of PtOEP increases from 0.3 to 30 wt%.

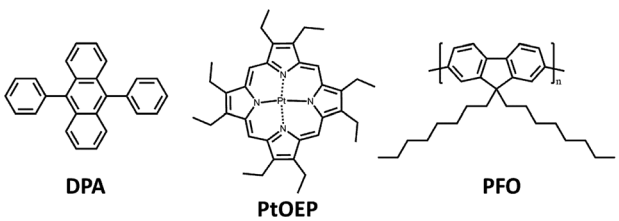

Scheme 1 (a) The chemical structures of DPA, PtOEP and PFO used in this study.

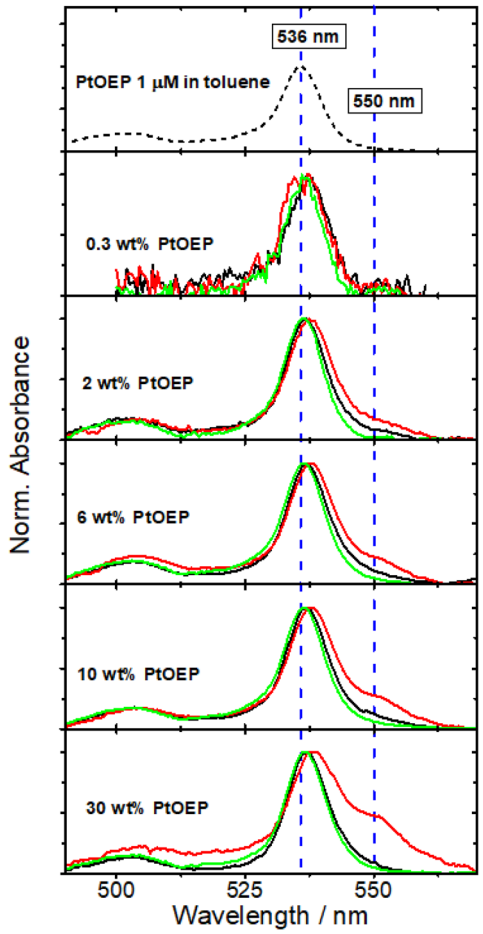

Fig. 1 Room-temperature composition dependent UV-vis absorption spectra of PS:PtOEP (black-solid line), DPA:PtOEP (red-solid line) and PS:DPA:PtOEP (green-solid line) films. For reference purposes the absorption spectrum of a dilute PtOEP solution in toluene is also presented (dashed black line).

Grazing incidence X-ray diffractometry

The degree of order in the studied PS:PtOEP, DPA:PtOEP and PS:DPA:PtOEP films was assessed by GIXRD measurements. For reference purposes, the X-ray diffraction (XRD) patterns of DPA powder and of a thermally evaporated DPA layer were also recorded (ESI Section, Fig. S.2†).

Concerning DPA, according to Salzillo *et al.*[78] three discrete polymorphs exist, and their formation is dictated by the different arrangements in the orientation and position of the pendant phenyl groups with respect to the main molecular π conjugated DPA core. All three DPA polymorphs crystallize in the monoclinic system; polymorph DPA-α belongs to the $C2/c$ (C_{2h}^6) space group whereas polymorphs DPA-β and DPA-γ belong to the $P2_1/\alpha$(C_{2h}^2) and $P2_1/n$ (C_{2h}^2) space groups, respectively. In terms of stability, DPA-α is thermodynamically stable whereas DPA-β and DPA-γ are metastable with marginal differences in their energies. DPA polymorphs-β and -γ can be obtained by rapid growth and their formation is facilitated by kinetically controlled processes such as sublimation. Polymorph DPA-α exhibits diffraction peaks at 2θ angles higher than 12°, whereas DPA polymorphs-β and -γ are easily identified by their expected XRD diffraction peaks at lower 2θ angles.[78] As for the PtOEP phase, PtOEP is known to crystallize in the triclinic system with space group $P1$.[87]

No diffraction signal is detected below 12° in the XRD diffractogram of DPA powder. In contrast, the thermally evaporated DPA film exhibits a diffraction signal at 8.45°, confirming the presence of metastable DPA polymorph species (see Fig. S.2 in the ESI Section).† Spin-coating DPA from solution facilitates the formation of DPA crystallites without the need to further process the obtained films, *e.g.*, by thermal annealing. As displayed in Fig. 2a, the GIXRD pattern of the pristine spin-coated DPA-only film exhibits a reflection at ~8.7°, resembling the XRD pattern of the evaporated DPA film. The SEM image presented in Fig. 2b resolves well-ordered fibrillar features on the surface of the DPA film made by spin-coating. Turning attention to PtOEP, a reflection at 8.8° is found in the GIXRD pattern of spin-coated PS:PtOEP 30 wt% from toluene solution (Fig. 2a), very similar to the XRD pattern of the PtOEP powder.[76] The different positions of the GIXRD reflections of DPA and PtOEP in the solid state allow for the discrimination of the crystalline DPA and PtOEP fractions that are present in DPA:PtOEP films.

Fig. 2c presents the overview of the GIXRD results collected for the PS:PtOEP, DPA:PtOEP and PS:DPA:PtOEP as-spun composites with a PtOEP content of 2 wt%. No reflections are found in the GIXRD patterns of the PS:PtOEP and PS:DPA:PtOEP systems. The absence of well-ordered DPA domains in the PS:DPA:PtOEP blend confirms the beneficial effect of using amorphous PS as a matrix to prevent the creation of DPA excimer sites.[39] Instead, the characteristic diffraction peak of the DPA crystallite at ~8.7° in the GIXRD diffractogram of the DPA:PtOEP composite verifies the formation of the kinetically entrapped DPA polymorph species.

In particular, polymorph-β of DPA is present in the DPA:PtOEP binary as proposed by the characteristic Raman signal at

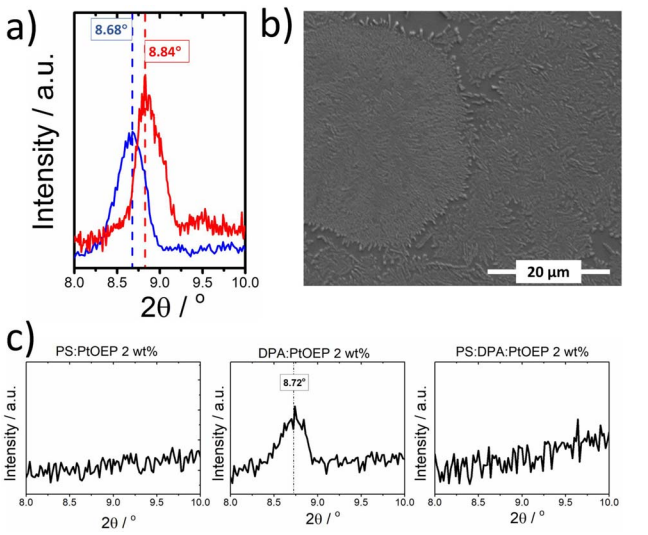

Fig. 2 (a) GIXRD patterns of DPA-only (blue line) and PS:PtOEP 30 wt% (red line) films, (b) SEM image of the DPA-only film, and (c) GIXRD patterns of PS:PtOEP, DPA:PtOEP and PS:DPA:PtOEP films with a 2 wt% PtOEP content. All films were characterized in their as-spun state after spin-coating from toluene solutions.

around 1300 cm^{-1} of complementary Raman spectra (ESI, Fig. S.3).† [78] Owing to the molecular rearrangement required for the interconversion of DPA polymorphs, we assume that under ambient conditions the DPA crystallites of the as-spun DPA:PtOEP remain entrapped in their metastable-β form.

For the three types of films, additional composition-dependent GIXRD measurements were performed (ESI, Fig. S.4)† for monitoring how the packing motifs of DPA and PtOEP are affected by varying the PtOEP content between 0.3 and 30 wt%. It was found that for all three types of films, the PtOEP phase is amorphous when the PtOEP contents is kept lower than 10 wt%. However, the structural order of the DPA phase in the films depends on the type of composite. In binary DPA:PtOEP, the characteristic DPA diffraction signal of polymorph-β at ~8.7° disappears when PtOEP loadings exceed 2 wt%. The absence of the thermodynamically stable DPA polymorph-α is confirmed by the GIXRD diffractogram of the DPA:PtOEP 30 wt% system that gave no evidence of diffraction peaks associated with DPA-α at 2θ angles higher than 12° (ESI, Fig. S.5).† In ternary PS:DPA:PtOEP, no GIXRD evidence was found for the presence of DPA crystalline domains across the whole monitored composition range.

Fourier transform infrared spectroscopy

Fourier transform infrared (FT-IR) spectroscopy was employed for gaining deeper insight into the PtOEP aggregation in the studied films. Due to the sensitivity of the FT-IR technique to subtle variations of molecular vibrations, its use provides indirect information about the presence of aggregate species.

For the PtOEP system, π-stacked dimers and higher order aggregates are expected to affect the intensity of the ethyl CH_2 scissors vibrational mode of PtOEP at 1458 cm^{-1}.[88,89] The FT-IR spectrum of the PtOEP powder is shown in Fig. 3a. In addition, Fig. 3b presents the composition dependent FT-IR spectra of the DPA:PtOEP binary system as processed from toluene. The acquired FT-IR spectra reveal that by increasing the PtOEP loading, the intensity of the PtOEP vibrational mode at 1458 cm^{-1} reduces relative to the rocking mode ρ_r of the PtOEP ethyl group (C_2H_5) at 960 cm^{-1}.[87,88,90] At high PtOEP loadings, *e.g.* when PtOEP is 30 wt%, the amplitude ratio of the 1458 cm^{-1}/960 cm^{-1} modes becomes comparable to that of PtOEP in powder (100%).

Time-gated photoluminescence spectroscopy

The PL properties of the PtOEP-based films with a 2 wt% PtOEP content were studied in the time-integrated and time-gated modes after pulsed laser photoexcitation at 532 nm. Time-gated PL acquisition was performed on the ns and the μs time-scale. For each of the PS:PtOEP, DPA:PtOEP and PS:DPA:PtOEP films, the acquired PL spectra are displayed in Fig. 4a–c respectively. As shown in these figures no differences are found between the time-integrated PL and the μs time-gated PL properties of the three films. Common to all PL spectra displayed in Fig. 4 is the feature of the PtOEP phosphorescence emission band centred at 644 nm. The additional PL bands detected at 780 nm and at 420 nm in the spectra of the DPA-based films (DPA:PtOEP in Fig. 4b and

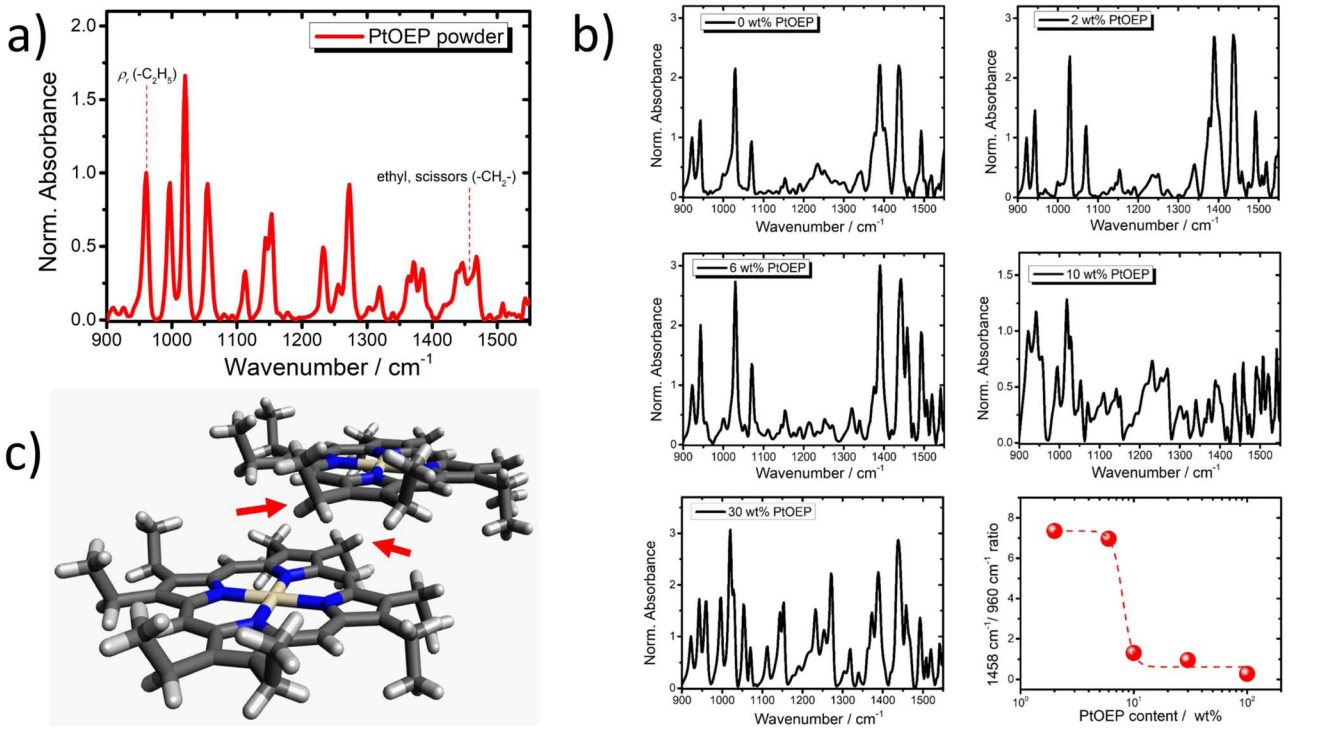

Fig. 3 (a) The FT-IR spectrum of PtOEP powder. (b) Composition dependent FT-IR spectra of binary DPA:PtOEP films as developed by toluene solutions. (c) Representation of a slip-stacked physical PtOEP dimer wherein the red arrows indicate the ethyl CH_2 scissors vibrational modes. Sphere color-code for atoms is C: grey, N: blue, Pt: light grey, and H: white.

PS:DPA:PtOEP in Fig. 4c), are attributed to the PtOEP triplet dimer PL emission and the up-converted DPA PL emission, respectively.[39] Regarding the ternary PS:DPA:PtOEP film, the spectral signatures of both features are more pronounced in the DPA:PtOEP binary system.

A different spectral overview is revealed on the ns time scale. At shorter delays after photoexcitation, PtOEP delayed fluorescence is detectable in all three PtOEP-based systems, centred in the 560–605 nm spectral region.[52] Strikingly, even in the PS:PtOEP film, the relative PL intensity of the 580 nm feature is comparable to the PtOEP phosphorescence emission intensity at 644 nm.

Fluence dependent measurements were further performed in time-integrated PL detection mode for the emissive PtOEP species of monomer phosphorescence at 644 nm, and dimer luminescence at 780 nm. Fig. 4d–f present the overview of the results when the spectrally integrated intensity of the two PL signals in each of the PS:PtOEP, DPA:PtOEP and PS:DPA:PtOEP films is plotted logarithmically as a function of laser pulse energy.

In the PS:PtOEP film (Fig. 4d), the response of both emissive species on fluence exhibits a slight deviation from linearity indicating that the triplet PtOEP excited states are prone to bimolecular annihilation effects. In the binary DPA:PtOEP film (Fig. 4e), the fluence dependent PL response is slightly different. The dependence of the 644 nm PL signal on photoexcitation is very close to unity, suggesting that Dexter energy transfer from triplet-excited PtOEP to DPA lowers triplet PtOEP exciton concentration and minimizes bimolecular effects. However, a nearly square-root dependence on photoexcitation intensity is found for the PL signal of the PtOEP triplet dimer at 780 nm, suggesting that exciton annihilation effects on triplet PtOEP dimer sites are severe. By dispersing the DPA:PtOEP 2 wt% composite in PS (Fig. 4f), the annihilation of PtOEP triplet photoexcitations is less intensive and the linear response of the 780 nm PL signal on photoexcitation intensity is restored. Overall, in PS:DPA:PtOEP both PtOEP monomer phosphorescence and dimer luminescence exhibit a fluence dependence comparable to that in the PS:PtOEP film.

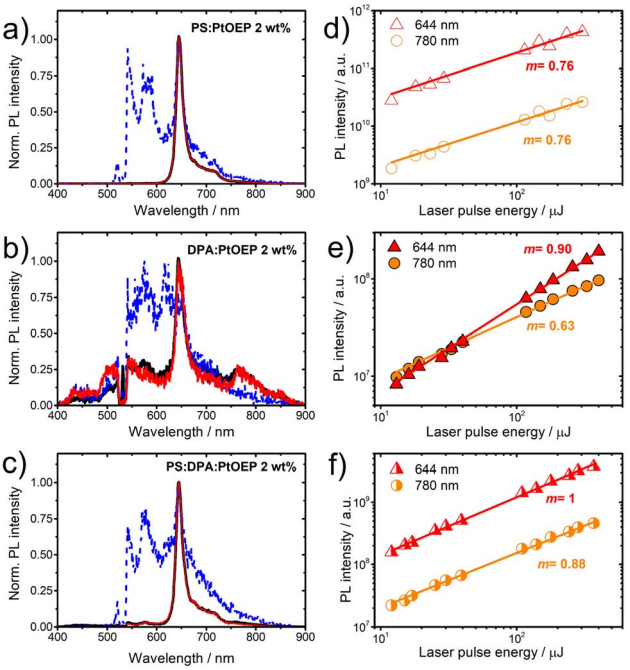

Fig. 4 Room temperature normalized PL spectra of spin-coated (a) PS:PtOEP, (b) DPA:PtOEP and (c) PS:DPA:PtOEP films cast from toluene solutions as registered in time-integrated (black-solid lines) and time-gated acquisition modes: prompt ns, 10 ns gate window (blue-dashed lines) and prompt μs, 10 μs gate window (red-solid lines). Photoexcitation intensity dependent PL spectral integrals of the time-integrated luminescence signal, as obtained at room temperature for toluene spin-coated films of (d) PS:PtOEP (open symbols), (e) DPA:PtOEP (filled symbols) and (f) PS:DPA:PtOEP (semi-filled symbols). The PL spectral area under the 644 nm (triangles) and 780 nm (circles) emission peaks is monitored, and for each dependence the obtained slope m is reported (see the text).

Time-gated photoluminescence kinetics

For the three types of PtOEP-based films we further recorded time-gated PL transients in a broad range of temperatures between 100 and 290 K after pulsed laser photoexcitation at 532 nm. For these measurements the excitation pulse energy was kept at 40 μJ. Fig. 5 presents the μs timescale transients of the triplet PtOEP monomer (Fig. 5a) and PtOEP dimer (Fig. 5b) phosphorescence of the PS:PtOEP, DPA:PtOEP and PS:DPA:PtOEP films at 180 K. The room temperature phosphorescence transients of these systems are presented in the ESI (Fig. S.6).† The effect of temperature on the processes responsible for the quenching of PtOEP phosphorescence in these film systems is discussed in the next session.

Fig. 5a suggests that no drastic differences are found in the kinetics the PtOEP monomer phosphorescence at 644 nm; the average PtOEP phosphorescence lifetime is found to be $\langle\tau_{PS:PtOEP}\rangle_{Ph.} = 100$ μs, $\langle\tau_{DPA:PtOEP}\rangle_{Ph.} = 93$ μs and $\langle\tau_{PS:DPA:PtOEP}\rangle_{Ph.} = 75$ μs (ESI Section, Table S.1).† Instead, under identical photoexcitation conditions and with respect to the PS:PtOEP and PS:DPA:PtOEP films, the PL transient of the PtOEP triplet dimer emission in DPA:PtOEP exhibits a significantly shorter lifetime. Based on the applied multiexponential fits, the average PtOEP triplet dimer phosphorescence lifetime at 180 K is found to be $\langle\tau_{PS:PtOEP}\rangle_{Ph.} = 97$ μs, $\langle\tau_{DPA:PtOEP}\rangle_{Ph.} = 45$ μs and

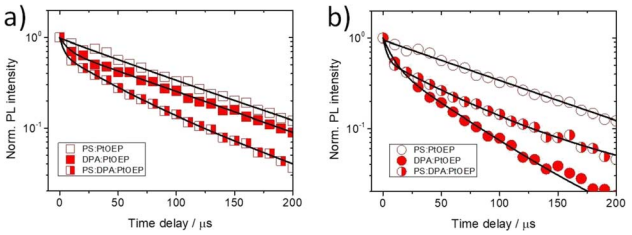

Fig. 5 Time-gated PL transients on the μs timescale at 180 K of (a) PtOEP monomer phosphorescence at 644 nm (squares), and (b) PtOEP triplet dimer phosphorescence at 780 nm (circles) for toluene spin-coated films of PS:PtOEP (open symbols), DPA:PtOEP (filled symbols) and PS:DPA:PtOEP (semi-filled symbols). In all cases the PL transients were acquired with a 10 μs gate window and a 10 μs gate step. Solid lines are exponential fits on the data.

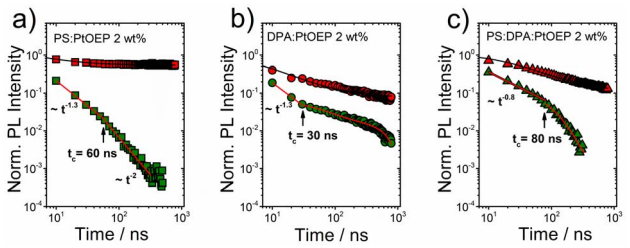

Fig. 6 Time-gated PL transients of PtOEP monomer phosphorescence at 644 nm (red symbols) and PtOEP delayed fluorescence at 580 nm (green symbols) on the ns timescale at 180 K for (a) PS:PtOEP, (b) DPA:PtOEP and (c) PS:DPA:PtOEP films spin-coated from toluene. In all cases the PL transients were acquired with a 10 ns gate window and a 10 ns gate step. Solid lines are fits on the data (see the text).

$\langle \tau_{PS:DPA:PtOEP} \rangle_{Ph.} = 96$ μs (ESI Section, Table S.2).† The two-fold acceleration of the dimer phosphorescence kinetics in DPA:PtOEP is in good agreement with the observed square-root PL fluence dependence of this system. In combination with the information derived from Fig. 4e, the PL kinetic data confirm the involvement of triplet PtOEP dimer sites in bimolecular TTA reactions.

Additional time-gated PL transients were recorded on the ns time scale. For each of the three systems Fig. 6 presents the PL transients of PtOEP delayed fluorescence (580 nm) in comparison with the corresponding kinetics of PtOEP monomer phosphorescence (644 nm) at 180 K.

The ns phosphorescence kinetics of the PtOEP monomer are in accordance with the integrated rate law of the PtOEP triplet excited state when both monomolecular and bimolecular events are considered.[52,54] As expected for a spin-forbidden radiative transition, at early times after photoexcitation, the PtOEP phosphorescence intensity remains virtually constant. Nevertheless, the PtOEP phosphorescence kinetics of the DPA:PtOEP and PS:DPA:PtOEP systems are found accelerated in respect to PS:PtOEP, due to the presence of the DPA component that facilitates Dexter energy transfer from triplet excited PtOEP to the triplet state of DPA. Focusing on the PtOEP delayed fluorescence, the intensity of the signal decays much faster in all three films. Moreover, the 580 nm PL decay of the PS:PtOEP film (Fig. 6a) is best described by a power-law function, thereby indicating the occurrence of a hopping process between progressively lower energy sites towards quasi-equilibrium. Typically, power-law PL kinetics reflect the dispersive relaxation of excitations within the DOS of an emissive ensemble of chromophores.[45,47,91] According to the Gaussian disorder model, a change in the power-law exponent α takes place at a characteristic transition time t_c, by becoming $\alpha = -2$. Considering that t_{c_0}, σ, and τ stand for the upper limit of the hopping time in the absence of energetic disorder, the standard deviation of the DOS, and the absolute temperature, respectively, t_c is given by eqn (1),[46,48] where k corresponds to the Boltzmann constant.

$$t_c = t_{c_0} \exp\left(\frac{2}{3}\frac{\sigma}{kT}\right)^2 \quad (1)$$

Overall, the characteristic power-law PL decay pattern that governs the kinetics of PtOEP delayed fluorescence in the three films is reminiscent of the dispersive relaxation pattern in the DOS of energetically disordered materials. For the PS:PtOEP film (Fig. 6a), at early times after photoexcitation the PL decay fits to a power-law function with $\alpha = -1.3$. However, at $t^{180K}_{cPS:PtOEP} = 60$ ns after photoexcitation it becomes steeper with $\alpha = -2$ thereby revealing the time where quasi-equilibrium is reached. In the case of the DPA:PtOEP (Fig. 6b) and PS:DPA:PtOEP (Fig. 6c) films, the 580 nm PL transients are best reproduced by the combination of a power-law decay at early times, and a multiexponential decay function at longer delay times. In these two films, t_c indicates the time where the PL decay function converts from a power-law to multiexponential and this conversion is influenced by the local environment of PtOEP. For the DPA:PtOEP system a power-law exponent of $\alpha = -1.3$ is found and the transition time is identified at $t^{180K}_{cDPA:PtOEP} = 30$ ns. Instead, for the PS:DPA:PtOEP system the power-law exponent is $\alpha = -0.8$ and the decay functional changes to multiexponential at $t^{180K}_{cPS:DPA:PtOEP} = 80$ ns.

When focusing on the biexponential regime of the 580 nm PL transients in DPA:PtOEP (Fig. 6b) and PS:DPA:PtOEP (Fig. 6c), the contribution of PtOEP phosphorescence intensity in this spectral region must also be considered. When one time constant of each biexponential fit is kept fixed to the average PtOEP phosphorescence lifetime of the blends, the second time constant can be determined. In doing so the fast PL decaying component of the 580 nm transients is found to be 55 ns and 70 ns, for DPA:PtOEP and PS:DPA:PtOEP respectively. The results suggest that after the transition time point t_c, the process responsible for the activation of PtOEP delayed fluorescence in the DPA:PtOEP and PS:DPA:PtOEP systems is still ongoing in parallel to the energy transfer process from triplet-excited PtOEP to DPA.

As a next step, the time-gated PtOEP delayed fluorescence transients of the PS:PtOEP film were recorded on the ns-time scale, at 140 K and 220 K. In Fig. 7, the overview of the registered PL decays informs that the quasi-equilibrium conditions are met at increasingly longer times as temperature lowers from 220 K to 140 K.

This is better shown in Fig. 8 where the dependence of the characteristic transition time $t^{T}_{cPS:PtOEP}$ on $1/T^2$ is presented for the PS:PtOEP film. When fitting the data of Fig. 8 with eqn (1), t_{c_0} is found to be 31 ns and $\sigma = 20$ meV.

Temperature dependent photoluminescence

For the PS:PtOEP, DPA:PtOEP and PS:DPA:PtOEP systems, the temperature dependent PL intensity of the three different PtOEP spectral features at 580 nm, 644 nm and 780 nm was monitored in the temperature range between 100 and 290 K. The PtOEP delayed fluorescence at 580 nm was followed on the ns time scale whereas the PtOEP phosphorescence at 644 nm and the triplet PtOEP dimer luminescence at 780 nm were followed on the μs time scale. In addition, the temperature dependent TTA-UC delayed luminescence intensity of DPA in the DPA:PtOEP and PS:DPA:PtOEP films was monitored on the

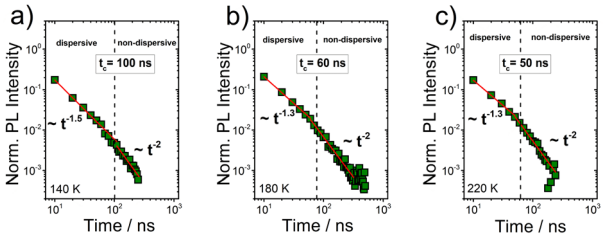

Fig. 7 Time-gated PL transients of PtOEP delayed fluorescence at 580 nm of the PS:PtOEP 2 wt% film spin-coated from toluene as measured at (a) 140 K, (b) 180 K and (c) 220 K. In all cases the PL transients were acquired with a 10 ns gate window and a 10 ns gate step. Solid lines are power-law fits on the data (see the text).

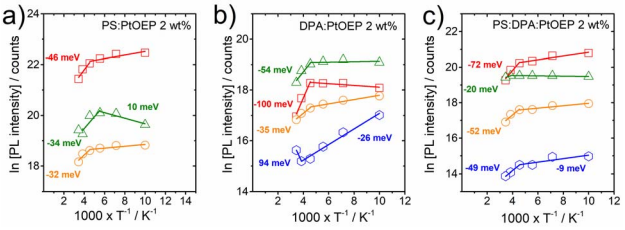

Fig. 9 Temperature-dependent PL intensity of PtOEP monomer phosphorescence at 644 nm (red symbols), PtOEP delayed fluorescence at 580 nm (green symbols), PtOEP triplet dimer phosphorescence (orange symbols), and DPA TTA-UC delayed fluorescence (blue symbols) in (a) PS:PtOEP, (b) DPA:PtOEP and (c) PS:DPA:PtOEP films spin-coated from toluene. Solid lines are Arrhenius fits on the data.

μs time scale. In all cases, the films were photoexcited at 532 nm with a pulse energy of 40 μJ. Fig. 9 displays the results for the PS:PtOEP (Fig. 9a), DPA:PtOEP (Fig. 9b) and PS:DPA:PtOEP (Fig. 9c) systems in an Arrhenius-type fashion.

The PtOEP phosphorescence intensity of each of the three films at 644 nm remains unchanged between 100 K and 180 K but at higher temperatures it is thermally deactivated. The deactivation energy within the 180–290 K range is determined to be $E_a = -46$ meV, $E_a = -100$ meV and $E_a = -72$ meV, for the PS:PtOEP, DPA:PtOEP and PS:DPA:PtOEP systems respectively. Due to the high concentration of PtOEP dimer trap sites in the DPA:PtOEP and PS:DPA:PtOEP systems the triplet excitons of the PtOEP phase are depleted by two discrete energy transfer channels: one towards the triplet DPA state and the second one towards the triplet PtOEP dimer sites. In contrast, only the channel associated with the energy transfer to the triplet PtOEP dimer sites is operative in the PS:PtOEP film. Both channels are facilitated by thermally activated exciton diffusion, and contribute to the reduction of the PtOEP phosphorescence intensity as temperature increases. In parallel, non-radiative relaxation losses of the triplet PtOEP exciton population are enhanced in all three systems as temperature increases. The significantly higher deactivation energy found for the DPA:PtOEP and PS:DPA:PtOEP films in the 180–290 K range reflects the thermally activated migration of PtOEP triplets towards the PtOEP/DPA interfaces where exergonic triplet energy transfer occurs towards the DPA triplet state manifold by quenching the PtOEP phosphorescence. The relatively stable PtOEP phosphorescence intensity of the three films at temperatures below 180 K indicates that both processes of non-radiative relaxation and triplet exciton diffusion within the PtOEP phase are kinetically hindered on the μs time scale. In this low temperature regime, only the fraction of the PtOEP triplet excitons formed in the vicinity of the interfaces with DPA and triplet dimer PtOEP sites can undergo triplet energy transfer, without the need for triplet exciton migration within the PtOEP phase.

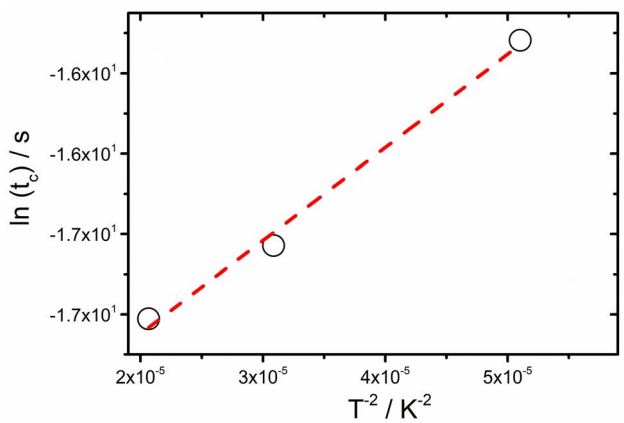

Fig. 8 Transition time (t_c) dependence on temperature, as determined by the ns timescale transient kinetics of the 580 nm PL signal of the PS:PtOEP 2 wt% film. Dashed line is the fit on the data according to eqn (1).

Focusing on the TTA-UC PL signal of the DPA:PtOEP and PS:DPA:PtOEP films, a severe PL quenching is observed in the low temperature regime. As temperature increases from 100 K to 220 K, the deactivation energy of the TTA-UC PL signal is found to be $E_a = -26$ meV and $E_a = -8.5$ meV for the DPA:PtOEP and PS:DPA:PtOEP films, respectively. Given the frustrated triplet PtOEP exciton migration in this temperature range, the registered TTA-UC delayed luminescence signal is attributed to TTA reactions between triplet DPA excitons activated *via* Dexter energy transfer in the vicinity of DPA/PtOEP interfaces.[39] The negative effect of temperature on the TTA-UC PL signal suggests that following the formation of the TTA-induced singlet state in DPA, non-radiative deactivation and PL quenching by exciton trapping to lower energy DPA excimer-like sites dominate.[39,52] Moreover, triplet excitons in the DPA phase are depleted by thermally activated monomolecular relaxation to the ground state instead of undergoing bimolecular TTA reactions in the triplet DPA manifold. This loss channel is verified by the temperature dependent response of the DPA phosphorescence signal in the 680 nm PL spectral region of the DPA:PtOEP and PS:DPA:PtOEP films (see Fig. S.7 in the ESI Section).† For DPA:PtOEP the deactivation energy of the DPA phosphorescence is $E_a = -17$ meV, whereas the corresponding deactivation energy of the PS:DPA:PtOEP film is less with $E_a = -9$ meV.

At temperatures above 180 K, the TTA-UC PL signal of the DPA:PtOEP film is enhanced in good agreement with the expected increase of DPA triplet concentration through triplet

energy transfer from PtOEP. In line with reduced PtOEP phosphorescence intensity, an activation energy of 94 meV is found for the TTA-UC PL intensity of DPA at temperatures higher than 220 K. In contrast, both of the TTA-UC and the phosphorescence intensity of DPA spectral features in the PS:DPA:PtOEP system are further quenched suggesting the dominance of non-radiative losses in the DPA triplet state population of the ternary PS:DPA:PtOEP film at high temperatures.

Regarding the triplet dimer PtOEP phosphorescence intensity in the 780 nm spectral region, all three films display a comparable response. For this emissive species no energy transfer to lower energy sites is possible and the expected thermally activated quenching channels are non-radiative relaxation and diffusion-controlled annihilation. At temperatures below 180 K, a common deactivation energy of $E_a \sim -7$ meV is found for all three systems. This is attributed to the thermally activated diffusion of triplet excitations in PtOEP dimer sites that facilitate annihilation reactions on the μs time scale. At higher temperatures, within the 180–290 K range, the triplet dimer PtOEP phosphorescence exhibits a deactivation energy of $E_a = -32$ meV, $E_a = -35$ meV, and $E_a = -52$ meV for the PS:PtOEP, DPA:PtOEP and PS:DPA:PtOEP films respectively.

Turning attention to the 580 nm PL signal on the ns time scale, the involvement of triplet PtOEP dimer sites in bimolecular TTA reactions is further verified. This becomes clearer when the antagonistic relationship between excited-state diffusion and non-radiative transitions is considered.[92] Both of the processes are thermally activated; however, temperature affects their magnitude in an opposite manner. Non-radiative transitions quench the PL intensity whereas diffusion-assisted TTA reactions result in PL enhancement. In all cases, within the 100–180 K range the PtOEP delayed fluorescence is resilient to temperature effects. Particularly for PS:PtOEP, an activation energy of $E_a = 10$ meV is found that reflects the positive effect of heating on the enhancement of delayed fluorescence *via* TTA. At temperatures higher than 180 K, the PtOEP delayed fluorescence intensity is quenched in all three systems. Within the 180–290 K range the determined deactivation energy of PtOEP delayed fluorescence is found to be $E_a = -34$ meV, $E_a = -54$ meV, and $E_a = -20$ meV, for the PS:PtOEP, DPA:PtOEP and PS:DPA:PtOEP films, respectively.

Dispersive excited state dynamics in unconventional solid-state photon up-converting composites

The above-described spectroscopic results (Fig. 4, 6 and 8) strongly suggest that the 580 nm delayed PtOEP fluorescence signal in the PL spectra of the DPA:PtOEP system relates to annihilation reactions between PtOEP excitations that undergo dispersive transport within the DOS of disordered PtOEP aggregates. For exploring whether a similar process is operative in other PtOEP-based composites, when DPA is not involved, a solution processed film prepared by PtOEP mixed with a blue-light emitting PFO derivative was investigated. In the PFO:PtOEP system, selective photoexcitation of PtOEP results in the generation of the TTA-UC PL of the PFO matrix,[54] even when photoexcitation of the film remains lower than the threshold intensity for the two-photon excitation of PFO.[93] According to GIXRD, the PtOEP phase of the PFO:PtOEP remains amorphous at a 6 wt% loading. However, the occurrence of PtOEP intermolecular interactions in the PFO matrix becomes evident from the PtOEP phosphorescence spectra of the blend on the μs time scale (ESI Section, Fig. S.8).†

Fig. 10a depicts the TA spectra of a 6 wt% blade-coated PFO:PtOEP film processed from toluene, after photoexcitation at 540 nm with a pulse energy of 1.1 μJ. Care was taken so that the repetition rate of the pump pulse (1 kHz) did not facilitate the build-up of triplet-excited PtOEP population during the measurement. Due to the superposition between the ground state absorption of PFO and PtOEP in the spectral range below 395 nm, the large optical density (>3.5) of the PFO:PtOEP film did not allow for the registration of the $\Delta T/T$ signal in this wavelength region. Instead, in the absence of PFO when a blade-coated PS:PtOEP 6 wt% control film was photoexcited in an identical manner (ESI Section, Fig. S.9),† a positive peak at 381 nm could be clearly resolved in the 0.1 ps delay $\Delta T/T$ spectrum. In good agreement with the spectral position of the PtOEP Soret-band,[85] the 381 nm feature of the PS:PtOEP film is attributed to the pump-induced change of PtOEP ground state population (ground state bleach, GSB).

As shown in Fig. 10a, the 0.1 ps delay $\Delta T/T$ spectrum of the PFO:PtOEP film is characterized by two positive sharp peaks at 400 nm and 533 nm, the latter accompanied by a shoulder at 500 nm. Both 500 nm and 533 nm features are in agreement with the $\Delta T/T$ spectra of the control PS:PtOEP 6 wt% film, matching spectrally with the Q-band of PtOEP. As such they are assigned to the GSB of PtOEP that is surrounded by excited state absorption (ESA). However, the positive peak at 400 nm cannot be attributed to the GSB of PtOEP. After 2 ps time delay, the sharp positive peak at 400 nm is overcome by the ESA signal of PtOEP, whereas the GSB signal of the PtOEP Q-band becomes more pronounced. As time evolves from 2 ps to 200 ps, the spectrum scarcely changes except for a 2 nm hypsochromic shift.

In order to elucidate the origins of the positive sharp peak at 400 nm in the early $\Delta T/T$ spectra of the PFO:PtOEP film, reference TA measurements were performed on a PFO-only film drop-casted from toluene. Fig. 10b presents the obtained $\Delta T/T$ spectra as received after photoexcitation of the PFO-only film at 387 nm. The spectra exhibit the characteristic features of PFO containing mixed phases of randomly coiled PFO (alpha-) and planarized PFO (beta-) chains.[94] At 1 ps delay, the $\Delta T/T$ spectrum consists of GSB (at 413 nm), SE (at 481 nm and 512 nm) and ESA at wavelengths above 521 nm. At longer time delays, fast decay of SE and broadening of ESA take place. This leads to a gradual 20 nm hypsochromic shift of the isosbestic point within 260 ps, thereby reflecting the interplay of singlet excitons and polaron pairs with different time decays.[95] Concomitantly, a negative $\Delta T/T$ dip at 439 nm develops tentatively ascribed to Stark shift due to changes in the polarization induced by photogeneration of charge pairs. In light of the acquired TA data of the PFO-only film, the sharp positive peak at 400 nm in the early $\Delta T/T$ spectra of the PFO:PtOEP film is attributed to the GSB of PFO, after selectively photoexciting the PtOEP blend component at 540 nm.

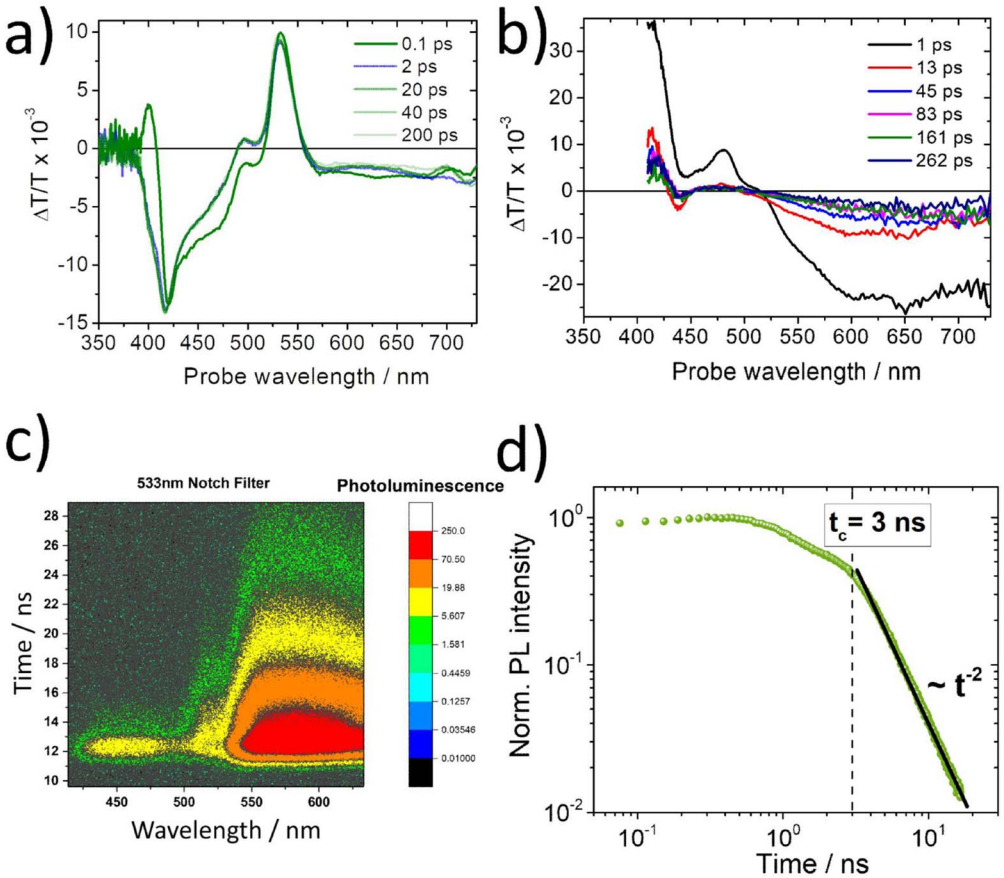

Fig. 10 Transient absorption ($\Delta T/T$) spectra of (a) PFO:PtOEP 6 wt% and (b) and PFO films processed from toluene at different pump delays. Pump wavelength in (a) was 540 nm and in (b) was 387 nm. (c) Streak camera image displaying the time-evolution of the PL spectra of a PFO:PtOEP film. (d) Room temperature TR-PL transients of the PFO:PtOEP film on the ns timescale, monitoring the PtOEP delayed fluorescence signal at 580 nm. Pump wavelength in (c) and (d) was 532 nm with a fluence of 627 μJ cm^{-2}. Solid line in (d) is a power-law fit on the data.

Next, the TR-PL response of a PFO:PtOEP 6 wt% film spin-coated from toluene solution was monitored on the ns time scale. The measurement was performed with a streak camera set-up after photoexcitation at 532 nm at room temperature. Fig. 10c verifies the detection of the up-converted PL signal by PFO in the 400–450 nm spectral region together with the PL signal of PtOEP at wavelengths beyond 550 nm. Fig. 10d presents the PtOEP delayed fluorescence PL transient at 580 nm of the PFO:PtOEP film. In good agreement with the results of the DPA:PtOEP systems, the PL transient exhibits a power-law decay pattern with a sharp transition at $t^{290K}_{cPFO:PtOEP} = 3$ ns after photoexcitation, where the power-law exponent becomes $\alpha = -2$.

Discussion

The collected results contribute to the effort to establish a robust correlation between the photophysical properties of the model PtOEP sensitizer with the microstructure of its composites in the solid state. Insight is gained by a GIXRD study about the effects of the PtOEP content on the microstructure of the DPA:PtOEP system. Three major PtOEP composition regions are identified wherein the packing motifs of the blend vary as the content of PtOEP is progressively increased. Region 1 corresponds to PtOEP contents up to 2 wt% where the DPA phase is semicrystalline, containing DPA-β polymorph species and the PtOEP phase remains amorphous. Region 2 corresponds to PtOEP contents between 2–10 wt%; here both DPA and PtOEP phases are amorphous. Finally, Region 3 begins from PtOEP contents of 10 wt% onwards wherein the PtOEP phase starts to become semicrystalline while DPA remains amorphous. SEM imaging verifies that irrespective of the degree of order in the studied films, PtOEP aggregates are formed across the whole monitored PtOEP composition range.

Three independent spectroscopic techniques probe the evolution of PtOEP aggregate formation in the PtOEP phase of the binary DPA:PtOEP blend. The UV-vis spectra of the DPA:PtOEP films (Fig. 1) display an increase in the relative intensity of the characteristic PtOEP dimer absorption band at 550 nm as the PtOEP content is gradually increased. Particularly for the DPA:PtOEP 2 wt% composition, the presence of PtOEP aggregates in the blend is further inferred by the detection of the PL spectral signature of the physical PtOEP dimer at 780 nm (Fig. 4b). Notably, the characteristic PL band of the PtOEP dimer is detectable even after dispersing the DPA:PtOEP 2 wt% system in PS (Fig. 4c). According to GIXRD (ESI Section, Fig. S.4)† both DPA and PtOEP phases of the PS:DPA:PtOEP composite are

amorphous (Region 2). Nevertheless, the persistence of the 780 nm PtOEP dimer PL band suggests that PtOEP demixing in PS:DPA:PtOEP is not entirely suppressed. Finally, the FT-IR results (Fig. 3) corroborate the occurrence of PtOEP aggregate formation in DPA:PtOEP. As the PtOEP content increases, a clear reduction in the aggregation-sensitive intensity of the PtOEP vibrational mode at 1458 cm^{-1} is observed with respect to the rocking mode ρ_r of the PtOEP ethyl group (C_2H_5) at 960 cm^{-1}. The suitability of the FT-IR technique as a diagnostic tool to monitor PtOEP aggregate formation in solid-state films was further tested by additional UV-vis and FT-IR spectroscopic measurements. Identical DPA:PtOEP 2 wt% composites were developed by using chloroform and chlorobenzene solutions. In these films, PtOEP aggregation is driven by the different rates of solvent evaporation and the PtOEP solubility. The solvent dependent UV-vis absorption spectra of the DPA:PtOEP films (ESI Section, Fig. S.10)† display a gradual increase in the concentration of the PtOEP dimer species as the volatility and the boiling point (T_b) of the solvent increase (chloroform T_b = 61.2 °C; toluene T_b = 110.6 °C; chlorobenzene T_b = 132 °C). In the same time, the reduction of the 1458 cm^{-1}/960 cm^{-1} mode amplitude ratio of the obtained FT-IR spectra confirms the increase in the PtOEP dimer species concentration in the blends.

Our study reveals that the as-spun DPA:PtOEP 2 wt% film comprises an amorphous phase of PtOEP aggregates dispersed within the semicrystalline DPA phase where DPA β-polymorph species are formed (Region 1). With these packing motif characteristics in the film, DPA excimer sites are activated.[39] However, the TTA-UC PL signal of the composite is mainly limited by inefficient triplet energy transfer from PtOEP to DPA, and by the thermally activated non-radiative relaxation of the DPA triplet excited state. Losses of the triplet PtOEP photoexcitations occur primarily due to triplet energy trapping in the physical PtOEP dimer sites and to bimolecular TTA reactions in the PtOEP phase. In agreement with the established Gaussian disorder model applied in organic semiconductor systems,[38,47,48] triplet PtOEP excitations undergo dispersive diffusion within the DOS of the triplet PtOEP dimer state and enable TTA reactions that activate the first singlet excited state of PtOEP on the ns time scale. As a result, the PtOEP delayed fluorescence signal is detected at 580 nm. The dispersive character of the bimolecular TTA process in PtOEP manifests in the power-law PL kinetics of the PtOEP delayed fluorescence (Fig. 6 and 7). The inhomogeneously broadened PL band of the PtOEP triplet dimer at 100 K is about 20 meV, very similar to the DOS width σ that is determined by applying eqn (1) on the data (Fig. 8). Moreover, the antagonistic relationship between non-radiative relaxation and thermally activated exciton diffusion in the DOS of PtOEP is revealed by the dependence of the TTA-induced delayed fluorescence of the PtOEP signal on temperature (Fig. 9).

The onset of bimolecular annihilation effects between PtOEP photoexcitation on dimer sites manifests in the μs timescale PL transient of the PtOEP triplet dimer emission at 780 nm. The PL lifetime of the PtOEP triplet dimer is substantially shorter with respect to the PS:PtOEP and PS:DPA:PtOEP systems (Fig. 5b and ESI, Fig. S.6).† The occurrence of TTA reactions between triplet PtOEP excitons in the PtOEP dimer ensemble is further proposed by the dependence of the 780 nm PL band on the photoexcitation intensity of the three composite systems. As the dependence comes closer to linearity (Fig. 4d–f), the PtOEP triplet dimer lifetime becomes longer.

The link between bimolecular TTA events on PtOEP triplet dimer sites and PtOEP delayed fluorescence generation is confirmed by control time-gated PL measurements. Time-gated PL spectra were acquired on the ns time scale for PS:PtOEP, DPA:PtOEP and PS:DPA:PtOEP blend systems spun from chloroform and chlorobenzene (ESI Section Fig. S.11).† For these systems, the relative intensity of the 580 nm PL signal becomes stronger as the dependence of the 780 nm triplet PtOEP dimer PL signal on photoexcitation intensity approaches a square-root functional form (ESI Section, Fig. S.12).†

The observation of dimer TTA-induced PtOEP delayed fluorescence in DPA:PtOEP is in line with a recent study on TTA-induced photocurrent generation in organic photodetection devices with thermally evaporated PtOEP photoactive layers.[76] Both processes point to a higher lying PtOEP state that is activated by TTA events and serves as a precursor for feeding the first singlet excited (S_1) and the charge transfer (CT) states of PtOEP. Considering the stabilization of PtOEP excitons in the triplet PtOEP dimer sites, the energy of the proposed TTA-activated higher lying state should be at least equal to ~3.18 eV, that is nearly isoenergetic with the second singlet excited state (S_2) of PtOEP. Previous TA results on neat PtOEP films[96] have shown how TTA reactions can activate the higher lying (d, d^*) $^3B_{1g}$ state, localized on the Pt^{II} metal centre[97] and energetically close to the S_2 and CT states of PtOEP. A question arises whether delayed PtOEP fluorescence originates from a charge recombination process that is driven by the sensitization of the $^3B_{1g}$ state *via* the TTA route. An answer can be provided by the spectroscopic results of the PFO:PtOEP 6 wt% blend film.

In the PFO:PtOEP system, PtOEP/PFO adduct species can be formed within co-aggregates in the blend,[27] yet no Dexter-type energy transfer is energetically favourable from triplet-excited PtOEP to PFO.[55] Since the S_1 state of PFO and the $^3B_{1g}$ state of PtOEP are isoenergetic, the TTA-UC luminescence of PFO in the PFO:PtOEP system should correspond to an electronic energy transfer process from triplet-excited PtOEP to PFO, based on a radiationless heteroatomic reverse intersystem crossing (rISC) transition.[98] However, previous results of electric-field induced TTA-UC PL quenching experiments on similar TTA-UC blends suggest that the rISC-pathway in PFO:PtOEP seems to be unlikely. Instead, ultrafast coupling between the $^3B_{1g}$ and CT states in PtOEP agree with the experimental data. In PFO:PtOEP the TTA-UC luminescence of PFO involves the sequence of: (i) TTA in PtOEP, (ii) activation of $^3B_{1g}$, (iii) ultrafast transition to CT and (iv) charge recombination to the S_1 of PFO, from where TTA-UC luminescence is produced.

At present, the spectroscopic study of the PFO:PtOEP system is in support of the proposed process. The detection of PtOEP delayed fluorescence in PFO:PtOEP confirms the occurrence of TTA in PtOEP. The power-law PL decay pattern of the PtOEP delayed fluorescence (Fig. 10d) is in good agreement with the

findings of the DPA:PtOEP system (Fig. 6). Yet, the onset of bimolecular TTA effects in PtOEP appears to take place on a much faster time scale. When PFO:PtOEP is photoexcited at 540 nm, a sharp positive peak at 400 nm in the early $\Delta T/T$ spectrum (Fig. 10a) is detected, implying that the S_1 state of PFO becomes activated within 100 fs after PtOEP photoexcitation. Therefore, intersystem crossing in PtOEP must occur on a time scale comparable with the temporal evolution of our TA set-up and the TTA-UC PL signal of PFO must be linked to the activation of the $^3B_{1g}$ state by bimolecular TTA reactions in the aggregated PtOEP phase of the blend.

Conclusions

In conclusion, our study reveals in detail how the photophysical properties of solid-state blends for TTA-UC applications are immensely affected by their layer microstructure. The findings on the benchmark DPA:PtOEP TTA-UC system identify aggregate formation of the PtOEP sensitizer that persists at low PtOEP contents, even when the composite is dispersed in a binder matrix. Further confirmation of PtOEP aggregate formation is obtained when FT-IR spectroscopy is used as a probing tool, in agreement with UV-vis spectroscopic characterization. The aggregation of PtOEP introduces energetic disorder in the DOS of the PtOEP component and it impacts the process of triplet exciton migration in the PtOEP phase of the DPA:PtOEP composite. Two key processes were monitored by time-gated PL spectroscopy and associated with the presence of the amorphous PtOEP aggregate species: (i) triplet exciton stabilization in PtOEP physical dimer sites and (ii) bimolecular TTA events in the aggregated PtOEP phase of the composite. As both processes occur prior to the triplet energy transfer step towards the triplet DPA manifold, they both affect negatively the TTA-UC efficiency and therefore have to be suppressed. The success in eliminating both processes can be validated efficiently when the PL spectral signature of PtOEP delayed fluorescence and the PL dynamics of the PtOEP dimer sites are directly probed. However, the findings on the PFO:PtOEP blend system suggest that a high concentration of sensitizer physical dimers may not be always detrimental to TTA-UC layers. Bimolecular TTA reactions in the phase of the PtOEP sensitizer facilitate photon management by alternative ultrafast excited state pathways, *e.g.* by activating higher lying metal-centred excited (d, d^*) states that can serve as precursors for TTA-UC PL and photocurrent generation.

For rationalizing the optimization of photophysical properties in TTA-UC layers, the formation of polymorph and aggregate species must be probed with high specificity. The herein proposed methodology has the capacity to establish rigorous structure/property correlations and to identify processing parameters that might be otherwise missed when a conventional perspective of photophysical characterization is adapted. The establishment of accurate probes aids the development of predictive processing protocols that in turn can produce high-performing TTA-UC composites with optimized microstructures.

The effective coupling of solid-state TTA-UC interlayers within the electronic structure of operational devices with a vertically stacked geometry is a nuanced and complex task. Our work wishes to encourage interdisciplinary collaborations between optical spectroscopy, materials science, exciton spin-state physics and device engineering. Based on this roadmap a new wave of transformative nanotechnology integration is anticipated.

Data availability

All data is in the corresponding ESI† section. There is no more to deposit.

Author contributions

H. G. and P. E. K. developed the solution processable films by spin coating. P. E. K. performed the composition dependent UV-vis spectroscopic measurements. H. G. performed the time-gated PL spectroscopic measurements under P. E. K.'s supervision. N. G. was in charge of film development by doctor-blading. Y. P. and G. A. undertook the development of the thermally evaporated DPA films. L. K. was in charge of the structural characterization of all films, analysed the corresponding data, and collected all SEM images. A. H. B. performed the ultrafast time-resolved photoluminescence (Streak camera) measurements under F. L.'s supervision. C. S. and J. C.-G. were in charge of transient absorption spectroscopic experiments and performed the analysis of the corresponding data. G. K. M. and P. F. performed the Raman spectroscopic measurements. C. C. T. and C. V. undertook the FT-IR measurements. S. A. was in charge of the DFT calculations. P. E. K. conceived the project, conceptualized the work, supervised the overall research activity, performed the analysis of the data and wrote the manuscript. All authors contributed to the completion of the manuscript and approved its final version.

Conflicts of interest

There are no conflicts to declare.

Acknowledgements

We thank Mr Marios Papageorgiou for his assistance during the sample preparation and acquisition of the composition-dependent FT-IR spectra. This work was co-funded by the European Regional Development Fund and the Republic of Cyprus through project EXCELLENCE/1216/0010 of the Cyprus Research and Innovation Foundation. This publication is based upon work supported by the King Abdullah University of Science and Technology (KAUST) Office of Sponsored Research (OSR) under Award No: OSR-CARF/CCF-3079. S. A. acknowledges support from the Deutsche Forschungsgemeinschaft (DFG, German Research Foundation) – through the project "MARS" (project number 446281755) and the Spanish Ministry of Science, Innovation and Universities (MICINN) through project RTI2018-101020-B-100. J. C.-G. and C. S. are grateful to

the China Scholarship Council (201608390023), to the Spanish Ministry of Science and Innovation (RTI2018-097508-B-I00, PID2021-128313OB-I00), the Regional Government of Madrid through projects NMAT2D-CM (S2018/NMT-4511), the program Proyectos Sinérgicos de I + D (Grant Y2018/NMT-5028 FULMATEN-CM), NANOCOV-CM (REACT-UE), and to the Campus of International Excellence (CEI). IMDEA Nanociencia acknowledges support from the Severo Ochoa Programme for Centres of Excellence in R&D (MINECO, grant CEX2020-001039-S).

References

1 M. B. Smith and J. Michl, *Chem. Rev.*, 2010, **110**, 6891–6936.
2 B. Kudisch, M. Maiuri, L. Moretti, M. B. Oviedo, L. Wang, D. G. Oblinsky, R. K. Prud'homme, B. M. Wong, S. A. McGill and G. D. Scholes, *Proc. Natl. Acad. Sci. U. S. A.*, 2020, **117**, 11289–11298.
3 C. F. Perkinson, M. Einzinger, J. Finley, M. G. Bawendi and M. A. Baldo, *Adv. Mater.*, 2022, **34**, 2103870.
4 D. G. Bossanyi, Y. Sasaki, S. Wang, D. Chekulaev, N. Kimizuka, N. Yanai and J. Clark, *JACS Au*, 2021, **1**, 2188–2201.
5 C. A. Parker and C. G. Hatchard, *Proc. Chem. Soc.*, 1962, 386–387.
6 S. Baluschev, T. Miteva, V. Yakutkin, G. Nelles, A. Yasuda and G. Wegner, *Phys. Rev. Lett.*, 2006, **97**, 143903.
7 N. J. Ekins-Daukes and T. W. Schmidt, *Appl. Phys. Lett.*, 2008, **93**, 063507.
8 A. Monguzzi, S. M. Borisov, J. Pedrini, I. Klimant, M. Salvalaggio, P. Biagini, F. Melchiorre, C. Lelii and F. Meinardi, *Adv. Funct. Mater.*, 2015, **25**, 5617–5624.
9 C. Li, C. Koenigsmann, F. Deng, A. Hagstrom, C. A. Schmuttenmaer and J.-H. Kim, *ACS Photonics*, 2016, **3**, 784–790.
10 S. P. Hill, T. Dilbeck, E. Baduell and K. Hanson, *ACS Energy Lett.*, 2016, **1**, 3–8.
11 Y. Y. Cheng, A. Nattestad, T. F. Schulze, R. W. MacQueen, B. Fückel, K. Lips, G. G. Wallace, T. Khoury, M. J. Crossley and T. W. Schmidt, *Chem. Sci.*, 2016, **7**, 559–568.
12 Y. L. Lin, M. Koch, A. N. Brigeman, D. M. E. Freeman, L. Zhao, H. Bronstein, N. C. Giebink, G. D. Scholes and B. P. Rand, *Energy Environ. Sci.*, 2017, **10**, 1465–1475.
13 S. Hamzawy, P. Wagner, J. K. Gallaher, T. W. Schmidt, A. J. Mozer and A. Nattestad, *J. Appl. Phys.*, 2021, **130**, 194501.
14 M. J. Bennison, A. R. Collins, B. Zhang and R. C. Evans, *Macromolecules*, 2021, **54**, 5287–5303.
15 T. Mori, S. Hamzawy, P. Wagner, A. J. Mozer and A. Nattestad, *J. Phys. Chem. C*, 2021, **125**, 14538–14548.
16 J. S. Lissau, M. Khelfallah and M. Madsen, *J. Phys. Chem. C*, 2021, **125**, 25643–25650.
17 W. G. J. H. M. van Sark, J. de Wild, J. K. Rath, A. Meijerink and R. E. I. Schropp, *Nanoscale Res. Lett.*, 2013, **8**, 81.
18 D. H. Weingarten, M. D. LaCount, J. van de Lagemaat, G. Rumbles, M. T. Lusk and S. E. Shaheen, *Nat. Commun.*, 2017, **8**, 14808.
19 D. Li, W.-Y. Lai, Q. Shao and W. Huang, *Inorg. Chem. Front.*, 2017, **4**, 1211–1214.
20 R. Singh, E. Madirov, D. Busko, I. M. Hossain, V. A. Konyushkin, A. N. Nakladov, S. V. Kuznetsov, A. Farooq, S. Gharibzadeh, U. W. Paetzold, B. S. Richards and A. Turshatov, *ACS Appl. Mater. Interfaces*, 2021, **13**, 54874–54883.
21 Y. Jiang, K. F. Li, K. Gao, H. Lin, H. L. Tam, Y.-Y. Liu, Y. Shu, K.-L. Wong, W.-Y. Lai, K. W. Cheah and W. Huang, *Angew. Chem., Int. Ed.*, 2021, **60**, 10007–10015.
22 S. Raišys, S. Juršėnas and K. Kazlauskas, *Solar RRL*, 2022, **6**, 2100873.
23 L. Wei, C. Fan, M. Rao, F. Gao, C. He, Y. Sun, S. Zhu, Q. He, C. Yang and W. Wu, *Mater. Horiz.*, 2022, **9**, 3048–3056.
24 P. E. Keivanidis, S. Baluschev, T. Miteva, G. Nelles, U. Scherf, A. Yasuda and G. Wegner, *Adv. Mater.*, 2003, **15**, 2095–2098.
25 S. Bagnich and H. Bässler, *Chem. Phys. Lett.*, 2003, **381**, 464–470.
26 F. Laquai, G. Wegner, C. Im, A. Busing and S. Heun, *J. Chem. Phys.*, 2005, **123**, 074902.
27 P. E. Keivanidis, S. Baluschev, G. Lieser and G. Wegner, *ChemPhysChem*, 2009, **10**, 2316–2326.
28 S. Raišys, S. Juršėnas, Y. C. Simon, C. Weder and K. Kazlauskas, *Chem. Sci.*, 2018, **9**, 6796–6802.
29 T.-A. Lin, C. F. Perkinson and M. A. Baldo, *Adv. Mater.*, 2020, **32**, 1908175.
30 S. Raišys, O. Adomėnienė, P. Adomėnas, S. Juršėnas and K. Kazlauskas, *Dyes Pigm.*, 2021, **194**, 109565.
31 S. Baluschev, V. Yakutkin, G. Wegner, B. Minch, T. Miteva, G. Nelles and A. Yasuda, *J. Appl. Phys.*, 2007, **101**, 023101.
32 P. B. Merkel and J. P. Dinnocenzo, *J. Lumin.*, 2009, **129**, 303–306.
33 R. Karpicz, S. Puzinas, V. Gulbinas, A. Vakhnin, A. Kadashchuk and B. P. Rand, *Chem. Phys.*, 2014, **429**, 57–62.
34 R. Vadrucci, C. Weder and Y. C. Simon, *J. Mater. Chem. C*, 2014, **2**, 2837–2841.
35 V. Sundström, *Prog. Quantum Electron.*, 2000, **24**, 187–238.
36 G. D. Scholes and G. Rumbles, *Nat. Mater.*, 2006, **5**, 683–696.
37 J. Cao, R. J. Cogdell, D. F. Coker, H.-G. Duan, J. Hauer, U. Kleinekathöfer, T. L. C. Jansen, T. Mančal, R. J. D. Miller, J. P. Ogilvie, V. I. Prokhorenko, T. Renger, H.-S. Tan, R. Tempelaar, M. Thorwart, E. Thyrhaug, S. Westenhoff and D. Zigmantas, *Sci. Adv.*, 2020, **6**, eaaz4888.
38 V. Jankus, E. W. Snedden, D. W. Bright, V. L. Whittle, J. A. G. Williams and A. Monkman, *Adv. Funct. Mater.*, 2013, **23**, 384–393.
39 H. Goudarzi and P. E. Keivanidis, *J. Phys. Chem. C*, 2014, **118**, 14256–14265.
40 G. M. Akselrod, P. B. Deotare, N. J. Thompson, J. Lee, W. A. Tisdale, M. A. Baldo, V. M. Menon and V. Bulović, *Nat. Commun.*, 2014, **5**, 3646.
41 A. Köhler and H. Bässler, *Prog. Quantum Electron.*, 2009, **71–109**, 71–109.

42 S. Raišys, K. Kazlauskas, S. Juršėnas and Y. C. Simon, *ACS Appl. Mater. Interfaces*, 2016, **8**, 15732–15740.
43 S. T. Hoffmann, H. Bässler and A. Köhler, *J. Phys. Chem. B*, 2010, **114**, 17037–17048.
44 S. Athanasopoulos, E. V. Emelianova, A. B. Walker and D. Beljonne, *Phys. Rev. B*, 2009, **80**, 195209.
45 M. Ansari-Rad and S. Athanasopoulos, *Phys. Rev. B*, 2018, **98**, 085204.
46 G. Schnönherr, R. Eiermann, H. Bässler and M. Silver, *Chem. Phys.*, 1980, **52**, 287–298.
47 S. C. J. Meskers, J. Hübner, M. Oestreich and H. Bassler, *J. Phys. Chem. B*, 2001, **105**, 9139–9149.
48 D. Hertel, H. Bässler, R. Guentner and U. Scherf, *J. Chem. Phys.*, 2001, **115**, 10007–10013.
49 S. T. Hoffmann, J.-M. Koenen, U. Scherf, I. Bauer, P. Strohriegl, H. Bässler and A. Köhler, *J. Phys. Chem. B*, 2011, **115**, 8417–8423.
50 S. T. Hoffmann, S. Athanasopoulos, D. Beljonne, H. Bässler and A. Köhler, *J. Phys. Chem. C*, 2012, **116**, 16371–16383.
51 S. Athanasopoulos, S. T. Hoffmann, H. Bässler, A. Köhler and D. Beljonne, *J. Phys. Chem. Lett.*, 2013, **4**, 1694–1700.
52 H. Goudarzi and P. E. Keivanidis, *ACS Appl. Mater. Interfaces*, 2017, **9**, 845–857.
53 S. Raišys, O. Adomėnienė, P. Adomėnas, A. Rudnick, A. Köhler and K. Kazlauskas, *J. Phys. Chem. C*, 2021, **125**, 3764–3775.
54 H. Goudarzi, S. Limbu, J. Cabanillas-González, V. M. Zenonos, J.-S. Kim and P. E. Keivanidis, *J. Mater. Chem. C*, 2019, **7**, 3634–3643.
55 P. E. Keivanidis, F. Laquai, J. W. F. Robertson, S. Baluschev, J. Jacob, K. Müllen and G. Wegner, *J. Phys. Chem. Lett.*, 2011, **2**, 1893–1899.
56 R. R. Islangulov, J. Lott, C. Weder and F. N. Castellano, *J. Am. Chem. Soc.*, 2007, **129**, 12652–12653.
57 A. Monguzzi, F. Bianchi, A. Bianchi, M. Mauri, R. Simonutti, R. Ruffo, R. Tubino and F. Meinardi, *Adv. Energy Mater.*, 2013, **3**, 680–686.
58 A. Turshatov, D. Busko, S. Baluschev, T. Miteva and K. Landfester, *New J. Phys.*, 2011, **13**, 083035.
59 J.-H. Kim, F. Deng, F. N. Castellano and J.-H. Kim, *Chem. Mater.*, 2012, **24**, 2250–2252.
60 A. Monguzzi, M. Frigoli, C. Larpent, R. Tubino and F. Meinardi, *Adv. Funct. Mater.*, 2012, **22**, 139–143.
61 C. Wohnhaas, V. Mailänder, M. Dröge, M. A. Filatov, D. Busko, Y. Avlasevich, S. Baluschev, T. Miteva, K. Landfester and A. Turshatov, *Macromol. Biosci.*, 2013, **13**, 1422–1430.
62 K. Katta, D. Busko, Y. Avlasevich, R. Muñoz-Espí, S. Baluschev and K. Landfester, *Macromol. Rapid Commun.*, 2015, **36**, 1084–1088.
63 R. Vadrucci, C. Weder and Y. C. Simon, *Mater. Horiz.*, 2015, **2**, 120–124.
64 K. Sripathy, R. W. MacQueen, J. R. Peterson, Y. Y. Cheng, M. Dvořák, D. R. McCamey, N. D. Treat, N. Stingelin and T. W. Schmidt, *J. Mater. Chem. C*, 2015, **3**, 616–622.
65 S. Mattiello, A. Monguzzi, J. Pedrini, M. Sassi, C. Villa, Y. Torrente, R. Marotta, F. Meinardi and L. Beverina, *Adv. Funct. Mater.*, 2016, **26**, 8447–8454.
66 J.-H. Kang, S. S. Lee, J. Guerrero, A. Fernandez-Nieves, S.-H. Kim and E. Reichmanis, *Adv. Mater.*, 2017, **29**, 1606830.
67 D. F. B. d. Mattos, A. Dreos, M. D. Johnstone, A. Runemark, C. Sauvée, V. Gray, K. Moth-Poulsen, H. Sundén and M. Abrahamsson, *J. Chem. Phys.*, 2020, **153**, 214705.
68 F. Saenz, A. Ronchi, M. Mauri, R. Vadrucci, F. Meinardi, A. Monguzzi and C. Weder, *Adv. Funct. Mater.*, 2021, **31**, 2004495.
69 F. Saenz, A. Ronchi, M. Mauri, D. Kiebala, A. Monguzzi and C. Weder, *ACS Appl. Mater. Interfaces*, 2021, **13**, 43314–43322.
70 H. Lee, M.-S. Lee, M. Uji, N. Harada, J.-M. Park, J. Lee, S. E. Seo, C. S. Park, J. Kim, S. J. Park, S. H. Bhang, N. Yanai, N. Kimizuka, O. S. Kwon and J.-H. Kim, *ACS Appl. Mater. Interfaces*, 2022, **14**, 4132–4143.
71 R. Enomoto, M. Hoshi, H. Oyama, H. Agata, S. Kurokawa, H. Kuma, H. Uekusa and Y. Murakami, *Mater. Horiz.*, 2021, **8**, 3449–3456.
72 M. Oldenburg, A. Turshatov, D. Busko, S. Wollgarten, M. Adams, N. Baroni, A. Welle, E. Redel, C. Wöll, B. S. Richards and I. A. Howard, *Adv. Mater.*, 2016, **28**(38), 8477–8482.
73 M. H. C. van Son, A. M. Berghuis, F. Eisenreich, B. de Waal, G. Vantomme, J. Gómez Rivas and E. W. Meijer, *Adv. Mater.*, 2020, **32**, 2004775.
74 T. Kashino, M. Hosoyamada, R. Haruki, N. Harada, N. Yanai and N. Kimizuka, *ACS Appl. Mater. Interfaces*, 2021, **13**, 13676–13683.
75 D. Beery, T. W. Schmidt and K. Hanson, *ACS Appl. Mater. Interfaces*, 2021, **13**, 32601–32605.
76 G. Antoniou, P. Yuan, L. Koutsokeras, S. Athanasopoulos, D. Fazzi, J. Panidi, D. G. Georgiadou, T. Prodromakis and P. E. Keivanidis, *J. Mater. Chem. C*, 2022, **10**, 7575–7585.
77 C. Quarti, D. Fazzi and M. Del Zoppo, *Phys. Chem. Chem. Phys.*, 2011, **13**, 18615–18625.
78 T. Salzillo, R. G. Della Valle, E. Venuti, A. Brillante, T. Siegrist, M. Masino, F. Mezzadri and A. Girlando, *J. Phys. Chem. C*, 2016, **120**, 1831–1840.
79 T. Kashino, R. Haruki, M. Uji, N. Harada, M. Hosoyamada, N. Yanai and N. Kimizuka, *ACS Appl. Mater. Interfaces*, 2022, **14**, 22771–22780.
80 A. Turshatov, D. Busko, N. Kiseleva, S. L. Grage, I. A. Howard and B. S. Richards, *ACS Appl. Mater. Interfaces*, 2017, **9**, 8280–8286.
81 F. Edhborg, H. Bildirir, P. Bharmoria, K. Moth-Poulsen and B. Albinsson, *J. Phys. Chem. B*, 2021, **125**, 6255–6263.
82 S. Mattiello, S. Mecca, A. Ronchi, A. Calascibetta, G. Mattioli, F. Pallini, F. Meinardi, L. Beverina and A. Monguzzi, *ACS Energy Lett.*, 2022, **7**, 2435–2442.
83 L. Cao, J. Li, Z.-Q. Zhu, L. Huang and J. Li, *ACS Appl. Mater. Interfaces*, 2021, **13**, 60261–60268.
84 R. Enomoto and Y. Murakami, *J. Mater. Chem. C*, 2023, DOI: **10.1039/D2TC04578H**.
85 A. K. Bansal, W. Holzer, A. Penzkofer and T. Tsuboi, *Chem. Phys.*, 2006, **330**, 118–129.

86 M. Hosoyamada, N. Yanai, T. Ogawa and N. Kimizuka, *Chem.–Eur. J.*, 2016, **22**, 2060–2067.
87 A. A. Abuelwafa, A. El-Denglawey, M. Dongol, M. M. El-Nahass and T. Soga, *Opt. Mater.*, 2015, **49**, 271–278.
88 J. R. Kincaid, M. W. Urban, T. Watanabe and K. Nakamoto, *J. Phys. Chem.*, 1983, **87**, 3096–3101.
89 A. S. Hinman and T. Olorunyolemi, *Can. J. Chem.*, 1993, **71**, 1975–1982.
90 O. Hisanobu, M. Naruhito, Y. Zen-ichi, T. James and N. Kazuo, *Bull. Chem. Soc. Jpn.*, 1971, **44**, 49–51.
91 T. Serevičius, R. Komskis, P. Adomėnas, O. Adomėnienė, G. Kreiza, V. Jankauskas, K. Kazlauskas, A. Miasojedovas, V. Jankus, A. Monkman and S. Juršėnas, *J. Phys. Chem. C*, 2017, **121**, 8515–8524.
92 R. Saxena, T. Meier, S. Athanasopoulos, H. Bässler and A. Köhler, *Phys. Rev. Appl.*, 2020, **14**, 034050.
93 G. Tsiminis, A. Ruseckas, I. D. W. Samuel and G. A. Turnbull, *Appl. Phys. Lett.*, 2009, **94**, 253304.
94 N. T. Lambeva, C. C. Mullen, X. Gao, Q. Wu, R. A. Taylor, Y. Tao and D. D. C. Bradley, *J. Polym. Sci., Part B: Polym. Phys.*, 2022, **61**(1), 83–93.
95 A. L. T. Khan, P. Sreearunothai, L. M. Herz, M. J. Banach and A. Köhler, *Phys. Rev. B: Condens. Matter Mater. Phys.*, 2004, **69**, 085201.
96 J. A. Hinke, T. J. Pundsack, W. A. Luhman, R. J. Holmes and D. A. Blank, *J. Chem. Phys.*, 2013, **139**, 101102.
97 U. Tripathy and R. P. Steer, *J. Porphyrins Phthalocyanines*, 2007, **11**, 228–243.
98 C. Richter, W. Hub, R. Traber and S. Schneider, *Photochem. Photobiol.*, 1987, **45**, 671–673.
99 Y. J. Bae, G. Kang, C. D. Malliakas, J. N. Nelson, J. Zhou, R. M. Young, Y.-L. Wu, R. P. Van Duyne, G. C. Schatz and M. R. Wasielewski, *J. Am. Chem. Soc.*, 2018, **140**, 15140–15144.
100 J. Kim, T. Batagoda, J. Lee, D. Sylvinson, K. Ding, P. J. G. Saris, U. Kaipa, I. W. H. Oswald, M. A. Omary, M. E. Thompson and S. R. Forrest, *Adv. Mater.*, 2019, **31**(32), 1900921.